Journal of Biomechanics 89 (2019) 48–56

Contents lists available at ScienceDirect

Journal of Biomechanics

journal homepage: www.elsevier.com/locate/jbiomech
www.JBiomech.com

An analytical poroelastic model of a spherical tumor embedded in normal tissue under creep compression

Md Tauhidul Islam, Raffaella Righetti *

Department of Electrical and Computer Engineering, Texas A&M University, College Station, TX 77840, USA

ARTICLE INFO

Article history:
Accepted 7 April 2019

Keywords:
Biomechanics
Biphasic theory
Cancer imaging
Elastography
Mechanopathology
Poroelasticity
Spherical model

ABSTRACT

An analytical model for a spherical poroelastic tumor embedded in normal poroelastic tissues under creep compression is presented in this paper. The tissue is modeled as a cylindrical sample containing a spherical inclusion having different material properties. Analytical expression for the volumetric strain generated inside the inclusion during creep compression is obtained. Error analysis is carried out by comparing the results from the developed analytical model with corresponding results obtained from an established finite element software for a number of samples with different material properties. The error is found to be below 2.5% for the samples with a small inclusion and 7% in the samples with a large inclusion. The analytical solutions reported in this paper can greatly impact elasticity imaging techniques aiming at reconstructing mechanical properties of tumors such as Young's modulus, Poisson's ratio, interstitial permeability and vascular permeability.

1. Introduction

The development of mathematical models that can accurately represent the mechanical behavior of cancers has been an active area of research for the past four decades. Several mechanical models incorporating the effects of osmotic and lymphatic pressure, vascular permeability and interstitial permeability on the mechanical behavior of tumors have been proposed (Baxter and Jain, 1989; Baxter and Jain, 1990; Baxter and Jain, 1991; Jain, 1998; Jain et al., 2007; Jain et al., 2014; Netti et al., 1997; Sarntinoranont et al., 2003; Swabb et al., 1974). Models considering the effect of elevated interstitial fluid pressure (IFP) and enhanced permeability and retention (EPR) on fluid transport mechanisms inside tumors (Netti et al., 1995; Netti et al., 2000; Stapleton et al., 2013; Swartz et al., 1999) as well as models considering the effect of residual strain and stress on the mechanical behavior of cancers (Byrne and Chaplain, 1996; Jones et al., 2000; Kyriacou et al., 1999) or tumor growth (Sciumè et al., 2014; Kremheller et al., 2018) have also been developed. These mathematical models were found clinically helpful to develop diagnostic instruments and treatment protocols for cancers. However, a common limitation of most of the aforementioned mechanical models is that they involve only the strains generated by the tumor's growth or by the fluid pressure or solid stress developed inside the tumor. These models do not apply to the case where the tissue is externally compressed as in many elasticity imaging technologies (Ophir et al., 1999).

After the seminal work by Eshelby (1957) on the mechanical behavior of an elastic inclusion inside another elastic material under remote load, many important studies have been reported, which focused on the mechanical behavior of an elastic/poroelastic inclusion inside another elastic/poroelastic material (Ateshian et al., 2007; Rice et al., 1978; Song et al., 2016b; Song et al., 2016a). Rice et al. (1978) reported a model of the displacements, strains and fluid pressure inside a poroelastic inclusion embedded in a poroelastic material. However, the solutions by Rice et al. (1978) are not in closed-form and require computation of a number of numerical integrals. In the works of Song et al. (2016b,a), the authors developed the expressions of the shear modulus for spherical and cylindrical poroelastic inclusions embedded inside another poroelastic material. The expressions for the displacement, stress and pore pressure are given in the Laplace domain, and no closed-form analytical expressions are obtained in the space or time domain, limiting their applicability to parameter estimation or other relevant analyses. In the work of Ateshian et al. (2007), analytical solutions for the strain components and fluid pressure have been developed in cylindrical coordinates for a spherical inclusion under compression, but the inclusion shape has been approximated as a cylinder.

Cryer (1963) was the first to report the analytical solution for the fluid pressure inside a uniform poroelastic sphere under

* Corresponding author.
E-mail address: righetti@ece.tamu.edu (R. Righetti).

https://doi.org/10.1016/j.jbiomech.2019.04.009
0021-9290/

application of a normal traction force over the surface of the sphere. He showed, theoretically, that, under sustained compression, the reduction of fluid pressure (due to the applied load) is not monotonic inside the poroelastic sphere. Rather, the fluid pressure increases initially with time and then it starts to decrease and eventually becomes zero. This effect is known as the "Mandel-Cryer effect". Cryer did not investigate the time evolution of the stress and strain during consolidation of the sphere. Later, a complete set of analytical expressions for the various stress and strain components inside the sphere was derived by Mason et al. (1991). A similar analysis of the consolidation of a sphere for large displacements/strains generated inside the sphere as a result of the application of high stress was reported by Gibson et al. (1989). These studies are applicable to a uniform poroelastic sphere and do not apply to a poroelastic sphere embedded inside another poroelastic material.

The mechanical behavior of human tissues has often been described using poroelastic models (Cowin and Doty, 2007; Pflaster et al., 1996), which are based on the poroelastic theory proposed by Biot (Biot, 1941; Biot, 1962; Cheng, 2016). Biot's theory is also at the basis of multi-phasic theories. According to these theories, a tissue is considered as a combination of at least two phases, i.e., a fluid phase and a solid phase (Ehlers and Markert, 2001; Suh and DiSilvestro, 1999). An example of multi-phasic theory is the biphasic theory developed by Kui, Lai and Mow (Mow and Lai, 1980; Mow et al., 2012; Mow et al., 1980; Mow et al., 1994). Using the biphasic theory, the first full analysis of the deformation behavior of a uniform poroelastic cylinder was reported by Mow et al. (1980) and later expanded by Armstrong et al. (1984). In the work of Armstrong et al. (1984), expressions of fluid pressure and strains were obtained for creep compression and stress relaxation inside a uniform poroelastic cylinder. Recently, four and five phase poroelastic models for tumor growth have been developed by Sciumè et al. (2014) and Kremheller et al. (2018). In the study of Sciumè et al. (2014), the extra-cellular matrix of the tumor is modeled as a deformable porous solid matrix with Green-elastic and elasto-visco-plastic material behavior. A dynamic vascular tumor model combining a multiphase porous medium framework for avascular tumor growth is proposed by Kremheller et al. (2018), where angiogenesis is modeled by treating the neovasculature as an additional phase of the material.

Human tissues are known to exhibit time-dependent compression-induced fluid pressure, stress and strain (Duck, 2013; Fung, 2013; Lakes, 1998; Leiderman et al., 2006). This is the underlying motivation at the basis of the development of ultrasound poroelastography (Konofagou et al., 2001; Righetti et al., 2004; Righetti et al., 2007). In poroelastography, the spatial and temporal distributions of the axial and lateral strains generated in a tissue under compression can be determined from the acquired ultrasound data using dedicated algorithms (Islam et al., 2018a; Nair et al., 2011). The spatial and temporal distributions of the lateral and axial strains are linked to the underlying mechanical properties of the poroelastic material (Islam et al., 2018d; Islam et al., 2018e).

In previous works, we have developed analytical models for the strains and fluid pressure inside non-uniform poroelastic samples by assuming that both the inclusion (tumor) and background (soft tissue) are of cylindrical shape (Islam et al., 2018c; Islam et al., 2018b; Islam et al., 2018d; Islam et al., 2018e). Most tumors, however, can be best approximated by spheres. An analytical model for the strains developed in a spherical inclusion embedded in a background with different poroelastic properties under creep compression would be helpful to better understand the mechanical behavior of tumors and estimate their mechanical properties from poroelastography data. However, such a model is not available yet. In this paper, we develop an analytical model of a spherical poroelastic inclusion embedded inside a cylindrical poroelastic sample under constant uniaxial compression. We then present a closed-form analytical solution of the volumetric strain inside the poroelastic inclusion and validate the solution using a commercial finite element simulation software.

Detailed nomenclature used in this paper is given in Table 1.

2. Problem formulation and analytical model

The cylindrical poroelastic sample containing a spherical inclusion used in the analysis reported in this paper is shown in Fig. 1 (A). This sample is used to represent a tumor embedded in normal tissue. In this figure, the method used to apply the external compression is also shown. Two rigid, parallel, impermeable compressor plates have been used to hold the sample and exert compression upon it. Perfect slip (i.e., frictionless) boundary conditions can be assumed to exist between the compressor plates and the sample (Berry et al., 2006; Armstrong et al., 1984; Zhou et al., 2015). The 'perfect slip' boundary conditions are important to ensure that the normal component of the fluid velocity at the interface of the compressor plate and the fluid in the sample is zero and the tangential component of the fluid velocity is unrestricted. Although these boundary conditions do not affect our analytical model of the volumetric strain inside the inclusion under the assumption of 'remote load' (Eshelby, 1957), these boundary conditions are important for the derivation of analytical models of strains and fluid pressure in uniform samples and cylindrical samples with cylindrical inclusions (Berry et al., 2006; Armstrong et al., 1984; Islam et al., 2018e; Islam et al., 2018d).

The boundary conditions for a poroelastography experiment are: (1) on the bottom plane of the cylindrical sample, there are no displacements; (2) on the right edge of the sample, there is no fluid pressure (Berry et al., 2006) and (3) a constant uniaxial stress is applied at the top boundary of the sample. The inclusion is assumed to be perfectly bonded to the background material.

Based on the theory of Eshelby, the applied uniaxial stress (σ) from the top of the sample in a poroelastography experiment (see Fig. 1(A)) is transferred over the full outer surface of the spherical inclusion (Eshelby, 1957). Therefore, when we are interested in the analysis of strains and fluid pressure inside the tumor, the problem can be thought as one of a poroelastic sphere under a uniform compressive/volumetric stress (σ_v) over its outer surface. Under these conditions, the volumetric strain and fluid pressure become functions of the spherical coordinate R (radius) and time t inside the poroelastic inclusion (Mason et al., 1991). Consequently, the problem can be simplified from a cylindrical coordinate system to a spherical coordinate system. Below, we derive the formulations for the various parameters inside the inclusion ($0 \leqslant R \leqslant a$) in spherical coordinates (Fig. 1(B)). .

The first basic equation for spherically symmetric poroelasticity is the continuity equation of the pore fluid, which can be written as (Islam et al., 2018d; Leiderman et al., 2006)

Table 1
Nomenclature.

Term	Symbol	Term	Symbol
Radius of inclusion	a	Radius of sample	b
Young's modulus of background	E_b	Young's modulus of inclusion	E_i
Poisson's ratio of background	ν_b	Poisson's ratio of inclusion	ν_i
Interstitial permeability of background	k_b	Interstitial permeability of inclusion	k_i
Microfiltration coefficient of background	χ_b	Microfiltration coefficient of inclusion	χ_i

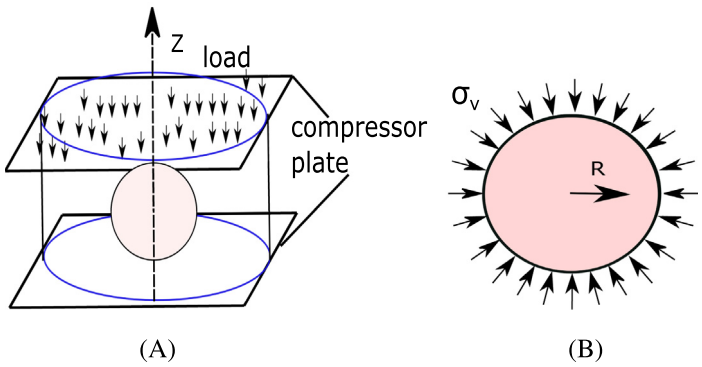

Fig. 1. (A) A schematic of a cylindrical sample of a poroelastic material with a spherical poroelastic inclusion of radius *a*. The sample is compressed between two compressor plates. The compression is applied along the negative *z* direction. (B) Schematic of the inclusion under compressive load.

$$\alpha\frac{\partial\epsilon}{\partial t}+S\frac{\partial p}{\partial t}+\chi_i p=k_i\left(\frac{1}{R}\frac{\partial^2(pR)}{\partial R^2}\right), \tag{1}$$

where ϵ is the volumetric strain and p is the fluid pressure inside the inclusion. α is Biot's coefficient, k_i is the interstitial permeability and S is the storage coefficient of the inclusion. Here the microfiltration coefficient of the inclusion $\chi_i=\chi_V+\chi_L$, with $\chi_V=\frac{L_{pV}S_V}{V_V}$ and $\chi_L=\frac{L_{pL}S_L}{V_L}$. L_{pV} and L_{pL} are the vascular and lymphatic permeabilities inside the inclusion. $\frac{S_V}{V_V}$ and $\frac{S_L}{V_L}$ are the surface area to volume ratio of the capillary and lymphatic walls, respectively. Under the assumption that $\chi_V\gg\chi_L,\chi_i$ becomes approximately equal to χ_V, i.e., $\chi_i\approx\chi_V$ (Netti et al., 1997; Leiderman et al., 2006). The storage coefficient S is defined as

$$S=\phi C_f+(\alpha-\phi)C_s, \tag{2}$$

where ϕ is porosity, C_f is the compressibility of the fluid, and C_s is the compressibility of the solid particles. In the case of incompressible constituents, $S=0$ and $\alpha=1$. It should be noted that Eq. (1) can be written for fluid pressure inside the inclusion only if the interstitial permeability of the inclusion is much lower than the interstitial permeability of the background, when the interstitial permeability has comparable or dominant effect as the vascular permeability on the mechanical behavior of the inclusion. Eq. (1) is always applicable for fluid pressure inside the inclusion when the inclusion's vascular permeability is dominant over its interstitial permeability.

Using $S=0,\alpha=1$, the continuity equation can be written as

$$\frac{\partial\epsilon}{\partial t}=k_i\left(\frac{\partial^2 p}{\partial R^2}+\frac{2}{R}\frac{\partial p}{\partial R}\right)-\chi_i p. \tag{3}$$

The volumetric strain ϵ inside the inclusion is related to the radial displacement u by

$$\epsilon=\frac{\partial u}{dR}+\frac{2u}{R}=\frac{1}{R^2}\frac{\partial\left(uR^2\right)}{\partial R}. \tag{4}$$

The second basic equation for poroelasticity is the equation of radial stress equilibrium, which can be expressed as

$$\frac{\partial\sigma_{RR}}{\partial R}+2\frac{\sigma_{RR}-\sigma_{TT}}{R}=0, \tag{5}$$

where σ_{RR} and σ_{TT} are the total stresses in radial and tangential directions. The total stresses can be separated into the effective stresses and the fluid pressure by

$$\sigma_{RR}=\sigma'_{RR}+p,\ \ \sigma_{TT}=\sigma'_{TT}+p. \tag{6}$$

The equation of radial stress equilibrium can be written now as

$$\frac{\partial\sigma'_{RR}}{\partial R}+2\frac{\sigma'_{RR}-\sigma'_{TT}}{R}+\frac{\partial p}{\partial R}=0. \tag{7}$$

Using Eq. (4) and the stress-strain relations

$$\sigma'_{RR}=-\left(K_i-\frac{2}{3}G_i\right)\epsilon-2G_i\frac{\partial u}{\partial R}, \tag{8}$$

$$\sigma'_{TT}=-\left(K_i-\frac{2}{3}G_i\right)\epsilon-2G_i\frac{u}{R}, \tag{9}$$

the equation of equilibrium can be expressed in terms of the volumetric strain as

$$\left(K_i+\frac{4}{3}G_i\right)\frac{\partial\epsilon}{\partial R}=\frac{\partial p}{\partial R}, \tag{10}$$

where K_i is the compression modulus of the inclusion in fully drained conditions, and G_i is its shear modulus.

Let the aggregate modulus be $H_{Ai}=K_i+\frac{4}{3}G_i$ (Armstrong et al., 1984). So, from Eq. (10), we can write

$$H_{Ai}\frac{\partial\epsilon}{\partial R}=\frac{\partial p}{\partial R}. \tag{11}$$

Integrating with respect to R, we obtain

$$\epsilon=\frac{1}{H_{Ai}}(p+Q), \tag{12}$$

where Q is an integration constant.

Let us assume that $p=p'e^{-H_{Ai}\chi_i t}, Q=Q'e^{-H_{Ai}\chi_i t}, \epsilon=\epsilon'e^{-H_{Ai}\chi_i t}$. ϵ' and p' depend on both space and time coordinates. Using these new variables in Eq. (3), we get

$$\frac{\partial\left(\epsilon'e^{-H_{Ai}\chi_i t}\right)}{\partial t}=k_i\left(\frac{\partial^2 p'}{\partial R^2}+\frac{2}{R}\frac{\partial p'}{\partial R}\right)e^{-H_{Ai}\chi_i t}-\chi_i p'e^{-H_{Ai}\chi_i t}. \tag{13}$$

Simplifying this equation, we obtain

$$-H_{Ai}\chi_i\epsilon'e^{-H_{Ai}\chi_i t}+e^{-H_{Ai}\chi_i t}\frac{\partial\epsilon'}{\partial t}=k_i\left(\frac{\partial^2 p'}{\partial R^2}+\frac{2}{R}\frac{\partial p'}{\partial R}\right)e^{-H_{Ai}\chi_i t}-\chi_i p'e^{-H_{Ai}\chi_i t}. \tag{14}$$

Removing $e^{-H_{Ai}\chi_i t}$ from both sides, this equation results in

$$-H_{Ai}\chi_i\epsilon'+\frac{\partial\epsilon'}{\partial t}=k_i\left(\frac{\partial^2 p'}{\partial R^2}+\frac{2}{R}\frac{\partial p'}{\partial R}\right)-\chi_i p', \tag{15}$$

which can be written as

$$-\chi_i(H_{Ai}\epsilon'-p')+\frac{\partial\epsilon'}{\partial t}=k_i\left(\frac{\partial^2 p'}{\partial R^2}+\frac{2}{R}\frac{\partial p'}{\partial R}\right). \tag{16}$$

Using $p' + Q' = H_{Ai}\epsilon'$ (Eq. (12)), we can write Eq. (16) as

$$-\chi_i Q' + \frac{\partial \epsilon'}{\partial t} = k_i\left(\frac{\partial^2 p'}{\partial R^2} + \frac{2}{R}\frac{\partial p'}{\partial R}\right). \tag{17}$$

Using $H_{Ai}\frac{\partial \epsilon'}{\partial R} = \frac{\partial p'}{\partial R}$ (Eq. (11)) and $H_{Ai}\frac{\partial^2 \epsilon'}{\partial^2 R} = \frac{\partial^2 p'}{\partial^2 R}$ (differentiating Eq. (11) with respect to R), we can write Eq. (17) as

$$-\chi_i Q' + \frac{\partial \epsilon'}{\partial t} = H_{Ai}k_i\left(\frac{\partial^2 \epsilon'}{\partial R^2} + \frac{2}{R}\frac{\partial \epsilon'}{\partial R}\right). \tag{18}$$

In this equation, Q' is a constant which depends on the boundary condition. If it is possible to find a solution for ϵ', which satisfies

$$\frac{\partial^2 \epsilon'}{\partial R^2} + \frac{2}{R}\frac{\partial \epsilon'}{\partial R} - \frac{1}{H_{Ai}k_i}\frac{\partial \epsilon'}{\partial t} = 0 \tag{19}$$

and all boundary and initial conditions, Q' becomes zero.

We now define the following dimensionless variables,

$$\hat{R} = \frac{R}{a}, \hat{t} = \frac{a^2 t}{H_{Ai}k_i}. \tag{20}$$

Using these dimensionless variables, we can write for ϵ' from Eq. (19)

$$\frac{\partial \epsilon'}{\partial \hat{t}} = \frac{\partial^2 \epsilon'}{\partial \hat{R}^2} + \frac{2}{\hat{R}}\frac{\partial \epsilon'}{\partial \hat{R}}. \tag{21}$$

To remove the partial derivative in $\hat{R}$, we introduce a new variable ψ, which is related to ϵ' as

$$\epsilon'\left(\hat{R}, t\right) = \frac{1}{\hat{R}}\psi\left(\hat{R}, t\right). \tag{22}$$

Eq. (21) can be written in terms of ψ as

$$\frac{\partial \psi}{\partial \hat{t}} = \frac{\partial^2 \psi}{\partial \hat{R}^2}. \tag{23}$$

Taking the Laplace transform of Eq. (23) and using the initial condition $\psi\left(\hat{R}, 0\right) = 0$, we obtain

$$\frac{\partial^2 \bar{\psi}}{\partial \hat{R}^2} - s\bar{\psi} = 0, \tag{24}$$

where $\bar{\psi}$ denotes the Laplace transform of ψ.

3. Solution for volumetric strain inside the inclusion

The general solution of Eq. (24) can be written as

$$\bar{\psi}\left(\hat{R}, s\right) = A(s)\cosh\left(\sqrt{s}\hat{R}\right) + B(s)\sinh\left(\sqrt{s}\hat{R}\right). \tag{25}$$

Therefore, using Eq. (22), $\bar{\epsilon}'$ can be written as

$$\bar{\epsilon}'\left(\hat{R}, s\right) = \frac{A(s)}{\hat{R}}\cosh\left(\sqrt{s}\hat{R}\right) + \frac{B(s)}{\hat{R}}\sinh\left(\sqrt{s}\hat{R}\right). \tag{26}$$

The first boundary condition for the volumetric strain inside the inclusion can be written as (Mason et al., 1991)

$$\hat{R} = 1, \quad \epsilon(1, \hat{t}) = \epsilon'(1, \hat{t}) = -\frac{(1+\nu_e)(1-2\nu_e)}{(1-\nu_e)}\frac{\sigma_v}{E_e}, \hat{t} > 0, \tag{27}$$

where ν_e is the lateral to axial strain ratio inside the inclusion, E_e is the effective Young's modulus calculated by taking the ratio of axial stress to axial strain inside the inclusion. The second boundary condition states that the volumetric strain is not infinite at the center of the inclusion, i.e.,

$$\hat{R} = 0, \quad |\epsilon(0, \hat{t})| < \infty, \hat{t} \geqslant 0. \tag{28}$$

Using Eqs. (27) and (28), we can write $\bar{\epsilon}'$ from Eq. (26) as (Verruijt, 2013; Cheng, 2016; Mason et al., 1991)

$$\bar{\epsilon}'\left(\hat{R}, s\right) = -\frac{\sigma_v}{E_e} \times \frac{(1+\nu_e)(1-2\nu_e)}{\left[(1-\nu_e)s + 2(1-2\nu_e)\sinh\left(\sqrt{s}\right) - 2(2-2\nu_e)\sqrt{s}\cosh\left(\sqrt{s}\right)\right]} \times \frac{\sinh\left(\sqrt{s}\hat{R}\right)}{\hat{R}}. \tag{29}$$

The inverse Laplace transform of this equation can be written as (Mason et al., 1991)

$$\epsilon'\left(\hat{R}, \hat{t}\right) = -\frac{3(1-2\nu_e)}{E_e}\sigma_v \times \left(1 + \frac{4}{3}\sum_{n=1}^{\infty}\frac{(1-2\nu_e)(1+\nu_e)}{\left[2(1+\nu_e)(1-2\nu_e) - (1-\nu_e)^2 x_n\right]} \times \frac{\sinh\left(\hat{R}\sqrt{x_n}\right)\exp(-x_n\hat{t})}{\hat{R}\sinh(\sqrt{x_n})}\right), \tag{30}$$

where x_n are the roots of the characteristic equation

$$C(x) = \tan(\sqrt{x}) - \frac{2(1-2\nu_e)\sqrt{x}}{[2(1-2\nu_e) - (1-\nu_e)x]} = 0. \tag{31}$$

Computation of the roots from the characteristic equation is shown in Fig. 2. Using Eq. (20), Eq. (30) can be written as a function of the time variable t and the space variable R as

$$\epsilon'(R, t) = -\frac{\sigma_v}{K_e} \times \left(1 + \frac{4}{3}\sum_{n=1}^{\infty}\frac{(1-2\nu_e)(1+\nu_e)}{\left[2(1+\nu_e)(1-2\nu_e) - (1-\nu_e)^2 x_n\right]} \times \frac{\sinh\left(\frac{R}{a}\sqrt{x_n}\right)\exp\left(-x_n\frac{H_{Ai}k_i t}{a^2}\right)}{\frac{R}{a}\sinh(\sqrt{x_n})}\right), \tag{32}$$

where $K_e = \frac{E_e}{3(1-\nu_e)}$. Eshelby's inclusion formulation can be used to calculate σ_v, which is equal to one-third of the axial stress inside the inclusion and K_e, i.e., E_e and ν_e from the applied load σ and the Young's modulus and Poisson's ratio of the inclusion and the background (Eshelby, 1957).

By changing the variable from ϵ' to ϵ and using the fact that $\epsilon(R, \infty) = \epsilon'(R, \infty) = -\frac{\sigma_v}{K_e}, 0 < R < a$, the equation for the volumetric strain inside the inclusion can be written as

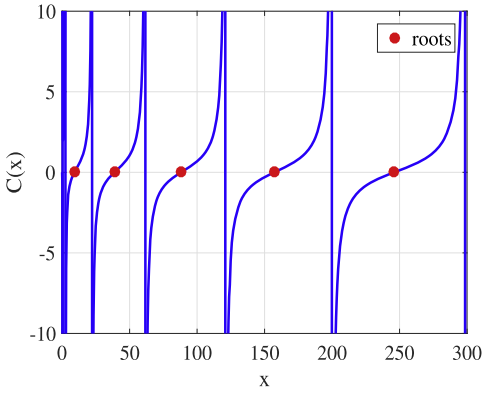

Fig. 2. Computation of roots from the characteristic equation.

$$\epsilon(R,t) = -\frac{\sigma_v}{K_e} \times \left(1 + \frac{4}{3}\sum_{n=1}^{\infty} \frac{(1-2\nu_e)(1+\nu_e)}{\left[2(1+\nu_e)(1-2\nu_e) - (1-\nu_e)^2 x_n\right]} \times \frac{\sinh(\frac{R}{a}\sqrt{x_n})\exp\left(-x_n \frac{H_{Ai}k_i t}{a^2}\right)}{\frac{R}{a}\sinh(\sqrt{x_n})} \exp(-H_{Ai}\chi_i t)\right). \quad (33)$$

4. Finite element simulations

The commercial finite element simulation software ABAQUS, Abaqus Inc, Providence, RI, USA has been used to validate the proposed theory (Documentation, 2006). The 'coupled pore fluid diffusion and stress analysis' module of ABAQUS has been used for this purpose (Documentation, 2006, 6.7.1). We have added the detailed theory of poroelastic simulation in ABAQUS in the Appendix.

We validate our theory in two steps. First, we show that our developed theory is accurate for computing the volumetric strain in a spherical sample under compressive stress (Fig. 1(B)) (see Appendix). Second, we show that our theory can also be used to compute the volumetric strain inside the inclusion in a cylindrical sample under creep compression (Fig. 1(A)). In this case, the compressive stress on the sphere has been computed using Eshelby's theory as described in Section (3).

4.1. Cylindrical samples

Due to the cylindrical and spherical symmetries of the cylindrical sample and inclusion, a 2D solution plane is analyzed in ABAQUS, as shown in Fig. 3. The dimensions of the cylindrical sample are 20 mm in radius and 40 mm in height. The radius of the spherical inclusion is assumed to be 3 mm in samples A-I and 7.5 mm in samples J-R. A Heaviside step load of 1 kPa is applied on top of the cylindrical samples.

We assume the following boundary conditions for the cylindrical samples: (1) the bottom plane of the sample is fixed, i.e., the axial displacement is zero at the bottom plane, (2) on the right side of the sample, the fluid pressure is zero and (3) the sample is compressed from the top, i.e., a constant uniaxial stress is present at the top boundary of the sample. A perfect bonding condition has been assumed between the inclusion and the background. Perfect slip (i.e., frictionless) boundary conditions between the compressor plates and the sample have been assumed.

4.2. Specifications for the samples

The vascular permeability in the samples is modeled using seepage coefficient as described in our previous work (Islam et al., 2018f). The specific weight of the fluid is taken as 1 Nm^{-3} to match the definitions of permeability in ABAQUS and in our developed theory. The CAX4RP mesh is used to model all the samples. The response of the simulated samples is recorded for 300 s at 1 s time intervals.

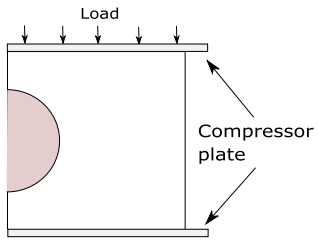

Fig. 3. The 2D solution plane for the three dimensional sample shown in Fig. 1(A).

Eighteen cylindrical samples with different material properties are simulated to analyze the theories developed in this paper. Nine of the eighteen cylindrical samples have inclusion radius of 3 mm and nine have radium 7.5 mm. The simulated samples are summarized in Tables 2 and 3. Young's modulus of the normal tissue is chosen as 32.78 kPa based on previous literature (Leiderman et al., 2006; Netti et al., 1997). As the tumors can have a broad range of Young's moduli (Rzymski and Opala, 2011; Zhi et al., 2007), up to ten inclusion-to-background contrasts are considered. Poisson's ratio values of 0.4, 0.45 and 0.47 for the tumors and normal tissues are used (Fung, 1993; Mpekris et al., 2017; Stylianopoulos et al., 2013). Based on previous literature (Netti et al., 2000; Swartz and Fleury, 2007), tumors can have a broad range of interstitial permeability. Therefore, different values of inclusion-to-background permeability contrast $(1, 2, 1000)$ are simulated in our study. The vascular permeability of the tumor and normal tissue are chosen based on the values reported by Leiderman et al. (2006) and Netti et al. (1997). Among the eighteen cylindrical samples, in samples A, G, J and P, the interstitial permeability is dominant over the vascular permeability inside the inclusion, whereas in samples C, F, H, L, O and Q, the vascular permeability is dominant over the interstitial permeability. In other samples, the interstitial permeability and vascular permeability have comparable effects inside the inclusion.

5. Parameter estimation

To demonstrate the feasibility of the proposed closed-form solution in estimation of different mechanical parameters, we generated clean signal of volumetric strain using Eq. (33) for the mechanical parameters of samples A, D and G and then added Gaussian noise of different SNRs (30, 40 and 60 dB) with the signal. We estimated the mechanical parameters from these noisy data and computed the error in estimated parameters as described in Appendix.

6. Error analysis

An error analysis is carried out to quantify the error between the results obtained using the developed analytical model and the corresponding results obtained using finite element method (FEM). The following formula is used to calculate the root mean squared error (RMSE) for the volumetric strain computed from the analytical model:

$$\text{RMSE} = \sqrt{\frac{\sum_{t}^{T}\sum_{r}^{R}\left(\epsilon_a(t,r) - \epsilon_f(t,r)\right)^2}{T \times R}} \times \frac{100 \times R}{\sum_{r}^{R}\epsilon_f(100,r)}, \quad (34)$$

Here, T is the total number of time samples considered, R is the number of points along the radial direction of the inclusion, ϵ_a is the volumetric strain estimated by the analytical model and ϵ_f is the volumetric strain estimated by the FEM. To generate the error values in Table 4, we used the first 100 samples, i.e., $T = 100$. We considered 3 radial positions, i.e., 0.5, 1.0 and 1.5 mm inside the small inclusion and 0.8, 2.4 and 4.0 mm inside the large inclusion of the cylindrical samples. This implies that $R = 3$.

7. Results

To obtain the instantaneous value of the volumetric strain inside the inclusion from the developed analytical model, we use the initial value theorem as applied to Eq. (29) shown in the Laplace domain. Putting $s \longrightarrow \infty$ in Eq. (29), we get $\epsilon(t = 0^+) = 0$. The instantaneous

Table 2
Description of the samples with inclusion radius of 3 mm.

Sample name	E_b (kPa)	E_i (kPa)	ν_b	ν_i	k_b ($m^4\ N^{-1}\ s^{-1}$)	k_i ($m^4\ N^{-1}\ s^{-1}$)	χ_b ($(Pas)^{-1}$)	χ_i ($(Pas)^{-1}$)
A	32.78	97.02	0.47	0.45	8.53×10^{-8}	1.8×10^{-13}	9.00×10^{-9}	5.00×10^{-9}
B	32.78	97.02	0.47	0.45	8.53×10^{-8}	5.103×10^{-13}	1.89×10^{-8}	5.67×10^{-8}
C	32.78	97.02	0.47	0.45	8.53×10^{-8}	2.04×10^{-14}	1.89×10^{-8}	5.67×10^{-8}
D	32.78	163.90	0.47	0.40	5.103×10^{-10}	5.103×10^{-13}	1.89×10^{-8}	5.67×10^{-8}
E	32.78	327.80	0.45	0.40	5.103×10^{-10}	5.103×10^{-13}	3.78×10^{-8}	5.67×10^{-8}
F	32.78	97.02	0.47	0.45	2.04×10^{-15}	2.04×10^{-15}	1.89×10^{-7}	5.67×10^{-7}
G	32.78	97.02	0.47	0.45	5.63×10^{-8}	1.188×10^{-13}	5.94×10^{-9}	3.3×10^{-9}
H	32.78	97.02	0.47	0.45	2.04×10^{-15}	2.04×10^{-15}	5.94×10^{-8}	2.83×10^{-7}
I	32.78	163.90	0.47	0.40	1.021×10^{-9}	1.021×10^{-12}	3.78×10^{-8}	1.134×10^{-7}

Table 3
Description of the samples with inclusion radius of 7.5 mm.

Sample name	E_b (kPa)	E_i (kPa)	ν_b	ν_i	k_b ($m^4\ N^{-1}\ s^{-1}$)	k_i ($m^4\ N^{-1}\ s^{-1}$)	χ_b ($(Pas)^{-1}$)	χ_i ($(Pas)^{-1}$)
J	32.78	97.02	0.47	0.45	1.125×10^{-9}	1.125×10^{-12}	9.00×10^{-9}	5.00×10^{-9}
K	32.78	97.02	0.47	0.45	3.189×10^{-9}	3.189×10^{-12}	1.89×10^{-8}	5.67×10^{-8}
L	32.78	97.02	0.47	0.45	1.276×10^{-10}	1.276×10^{-13}	1.89×10^{-8}	5.67×10^{-8}
M	32.78	163.90	0.47	0.40	3.189×10^{-9}	3.189×10^{-12}	1.89×10^{-8}	5.67×10^{-8}
N	32.78	327.80	0.45	0.40	3.189×10^{-9}	3.189×10^{-12}	3.78×10^{-8}	5.67×10^{-8}
O	32.78	97.02	0.47	0.45	1.276×10^{-14}	1.276×10^{-14}	1.89×10^{-7}	5.67×10^{-7}
P	32.78	97.02	0.47	0.45	0.742×10^{-9}	0.742×10^{-12}	5.94×10^{-9}	3.3×10^{-9}
Q	32.78	97.02	0.47	0.45	2.54×10^{-14}	1.27×10^{-14}	5.94×10^{-8}	2.83×10^{-7}
R	32.78	163.90	0.47	0.40	6.38×10^{-9}	6.38×10^{-12}	3.78×10^{-8}	1.134×10^{-7}

Table 4
Root mean squared error between results from analytical model and FEM in cylindrical samples.

Sample name	RMSE (%)	Sample name	RMSE (%)
A	0.87	J	2.05
B	0.87	K	2.52
C	0.98	L	1.22
D	1.77	M	2.93
E	2.48	N	6.84
F	0.92	O	2.17
G	0.88	P	2.08
H	0.91	Q	2.19
I	1.13	R	2.91

values of total radial and circumferential stresses inside and outside the inclusion become zero at the instant the strain/load is applied. Thus, the volumetric strain is zero. However, the effective stress on the solid matrix is not zero, which triggers the recoiling behavior. The recoiling nature of the solid phase induces a pressure gradient, which facilitates fluid exudation. When the solid matrix is fully relaxed, the volumetric strain depends only on the bulk modulus of the inclusion and the applied strain, which can be found by letting $t \longrightarrow \infty$ in Eq. (33). The volumetric strain at steady state can be found as $-\frac{\sigma_\nu}{K_e}$. Therefore, at time $t = 0^+$, the inclusion behaves as an incompressible solid with Poisson's ratio of 0.5 while, at steady state, the inclusion behaves as a compressible solid with Poisson's ratio equal to the one of the solid matrix.

7.1. Cylindrical samples

Analytical and corresponding FEM results for nine simulated samples (A-I) are shown in Figs. 4–6. Figs. 4–6(A)-(C) show the time evolution of the volumetric strain inside the inclusion in samples A-I. From these figures we see that, for all samples, at time $t = 0^+$, the volumetric strain inside the inclusion is 0. As time progresses, the negative volumetric strain increases and reaches a value that is dependent on the elastic compression modulus of the inclusion and the compression applied to the sample. Good visual correspondence between analytical and FEM results can be observed for all simulated samples.

In samples A and G, we see that the volumetric strain varies with space inside the inclusion. This is because, in these samples, the interstitial permeability is dominant over the vascular permeability inside the inclusion. If the interstitial permeability is dominant over the vascular permeability, the fluid needs to pass a distance to exude, which gives rise to non-uniform fluid flow and pressure inside the inclusion. This makes the volumetric strain spatially dependent as the volumetric strain depends on the fluid pressure inside the inclusion. On the other hand, in samples C, F and H, we see that the volumetric strain does not vary with space. This is because in these samples, the vascular permeability is dominant over the interstitial permeability. As the capillary vessels are distributed throughout the inclusion (which is the case in real tumors) and, as a result, the fluid flow and pressure are the same everywhere inside the inclusion. In other samples (B, D, E and I), as the interstitial permeability and vascular permeability have comparable effects, the volumetric strain has much lower spatial variation than that in samples A and G.

In Table 4, the error in the computed volumetric strain from the developed analytical model in comparison to that from the FEM is reported. From this table, we see that the error is overall very small ($< 2.5\%$) in samples with small inclusion, which suggests the correctness of the proposed model. The error increases inside the samples, where the inclusion and background have high Young's modulus and/or Poisson's ratio contrast.

The errors in computed volumetric strain in samples J-R are also shown in Table 4. We see that overall, the error increases (as high as 6.84%) in samples with large inclusion in comparison to the samples with small inclusion. In the samples with large inclusion, the assumption of remote load may not be fully satisfied. The large

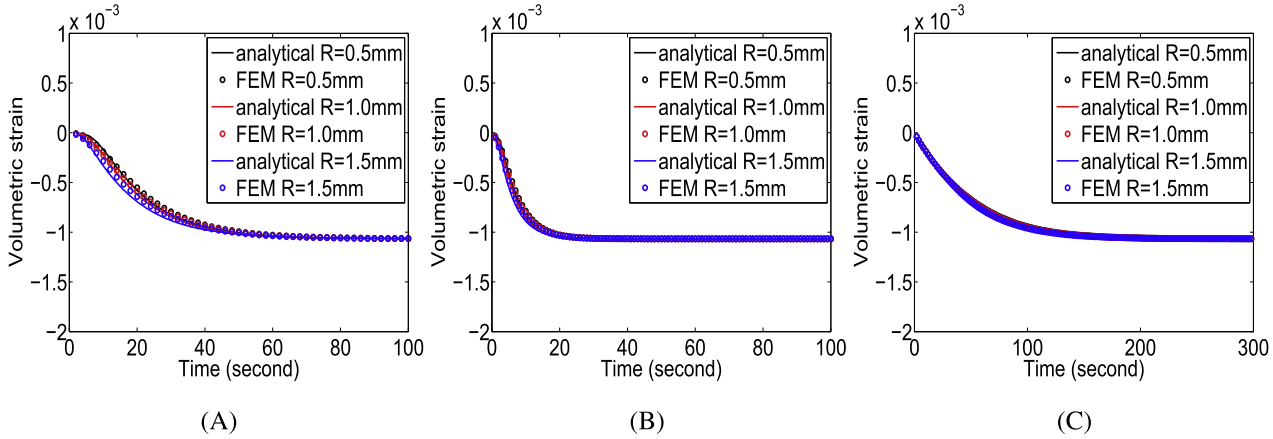

Fig. 4. Volumetric strain at different positions inside the inclusion of samples A (A), B (B) and C (C).

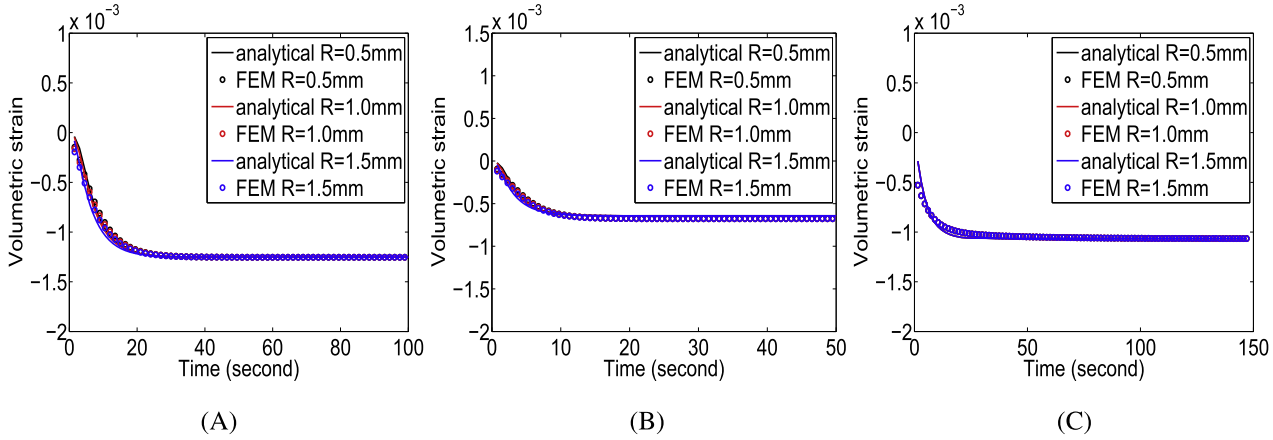

Fig. 5. Volumetric strain at different positions inside the inclusion of samples D (A), E (B) and F (C).

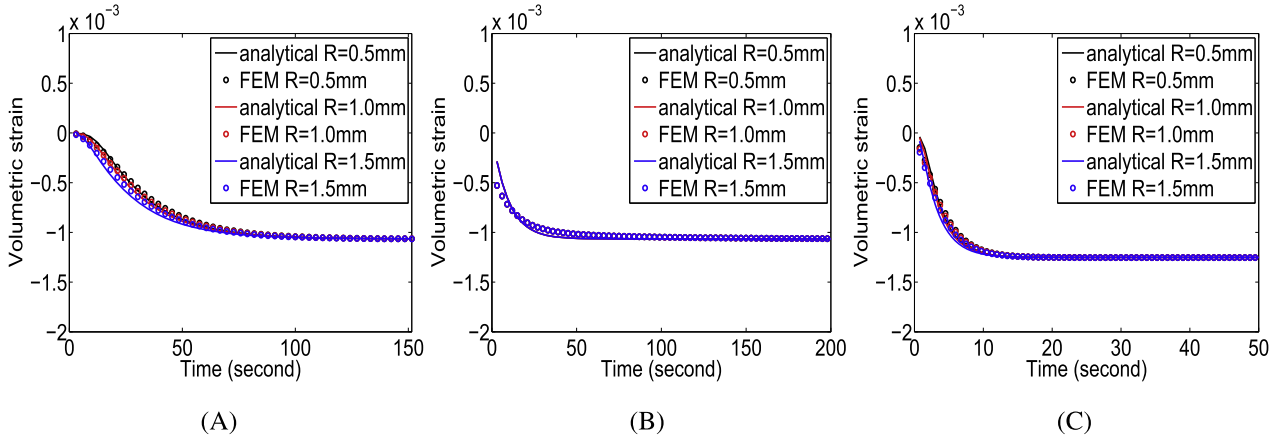

Fig. 6. Volumetric strain at different positions inside the inclusion of samples G (A), H (B) and I (C).

errors in these samples are results of the violation of the assumption of remote load.

We reported the error in estimated mechanical parameters from the noisy data created from the proposed analytical solution in the Appendix. The error is found to be small at all SNRs, i.e., $< 0.05\%, < 2\%$ and $< 10\%$ in estimation of Young's modulus, interstitial permeability and vascular permeability.

8. Discussion

In this paper, we present and analyze an analytical model for a spherical solid tumor embedded in normal tissue under creep compression. By solving the poroelastic differential equations from the model, we derive the closed-form analytical expression for the volumetric strain inside the inclusion.

In the developed analytical model, we considered a creep experiment. However, the developed expression of volumetric strain (Eq. (33)) is also applicable to stress relaxation experiments assuming that all other conditions remain the same. In this case, the applied stress in Eq. (33) would need to be calculated through $\sigma = E_b\epsilon_0$, where ϵ_0 is the uniaxial strain applied to the sample. We have reported the analytical expression of the volumetric strain inside the inclusion only. The analytical expression of the strains inside the background of the sample far away from the inclusion can be calculated using the theory developed in Leiderman et al. (2006).

The developed analytical model and solutions can have a strong impact on quantitative medical imaging technologies, such as quasi-static ultrasound and magnetic resonance elastography. They can be used to estimate mechanical parameters of cancers such as Young's modulus, Poisson's ratio, interstitial permeability and vascular permeability. These mechanical parameters are of great clinical significance as they are important markers of malignancy in tumors and can greatly affect efficacy of therapies (Baxter and Jain, 1989; Rzymski et al., 2010; Sarntinoranont et al., 2003; Sinkus et al., 2005; Swabb et al., 1974; Zhi et al., 2007). The analytical expressions also allow determination of the time dependent volumetric strain in a tumor when material properties are known.

The main limitations of the proposed analytical model reside in the assumptions undertaken to develop the theories. First, the proposed analytical model is developed under the assumption of remote load, which requires the inclusion size to be much smaller than the size of the sample. In our recent work (Islam et al., 2018g), we found that this assumption holds in practical elastography experiments, and parameters (Young's modulus, Poisson's ratio) reconstructed in a breast phantom based on this assumption match with the corresponding parameters provided by the manufacturer. Second, the developed model is not applicable when the interstitial permeability has dominant/comparable effect on the strains and fluid pressure in comparison to the vascular permeability inside the tumor and the interstitial permeability of the normal tissue is lower or comparable to the interstitial permeability of the tumor. However, based on reported values of interstitial permeability and vascular permeability of tumors and normal tissues (Baxter and Jain, 1989; Baxter and Jain, 1990; Baxter and Jain, 1991; Netti et al., 1995; Netti et al., 1997; Netti et al., 2000; Sarntinoranont et al., 2003; Swabb et al., 1974), this scenario is unlikely to occur in most cancers.

In our problem formulation, the spherical inclusion is shown at the center of the cylindrical sample. However, the developed theory is applicable for an inclusion located anywhere in the sample as long as the 'remote load' assumption is satisfied and the applied load acts uniformly on the surface of the inclusion (Eshelby, 1957). The sample can also be of any shape but should be sufficiently large to satisfy the 'remote load' assumption and should be perfectly flat (horizontally) where the load is applied. Finally, we note that, although the proposed model has been developed for application in ultrasound poroelastography, it can also be useful in fields such as rock mechanics, ceramic engineering, soil and petroleum engineering, where the scenario of a poroelastic inclusion embedded inside a poroelastic material frequently arises.

9. Conclusion

An analytical model for a spherical poroelastic inclusion embedded inside a cylindrical poroelastic sample under constant pressure is developed, and a closed-form analytical expression for the volumetric strain inside the spherical inclusion is derived. This model can be thought as representing a spherical solid tumor embedded inside normal tissues in an elastography experiment. On this regard, the developed model can be useful to reconstruct material properties of the tumor, which are helpful for diagnosis and treatment of cancers.

Conflict of Interest

The authors declare no conflict of interest.

Acknowledgments

This work was funded in part by the U.S. Department of Defense under grant W81XWH-18-1-0544 (BC171600).

Appendix A. Supplementary material

Supplementary data associated with this article can be found, in the online version, at https://doi.org/10.1016/j.jbiomech.2019.04.009.

References

Armstrong, C., Lai, W., Mow, V., 1984. An analysis of the unconfined compression of articular cartilage. J. Biomech. Eng. 106, 165–173.
Ateshian, G.A., Costa, K.D., Hung, C.T., 2007. A theoretical analysis of water transport through chondrocytes. Biomech. Model. Mechanobiol. 6, 91–101.
Baxter, L.T., Jain, R.K., 1989. Transport of fluid and macromolecules in tumors. I. Role of interstitial pressure and convection. Microvasc. Res. 37, 77–104.
Baxter, L.T., Jain, R.K., 1990. Transport of fluid and macromolecules in tumors. II. Role of heterogeneous perfusion and lymphatics. Microvasc. Res. 40, 246–263.
Baxter, L.T., Jain, R.K., 1991. Transport of fluid and macromolecules in tumors. IV. A microscopic model of the perivascular distribution. Microvasc. Res. 41, 252–272.
Berry, G.P., Bamber, J.C., Armstrong, C.G., Miller, N.R., Barbone, P.E., 2006. Towards an acoustic model-based poroelastic imaging method: I. Theoretical foundation. Ultrasound Med. Biol. 32, 547–567.
Biot, M.A., 1941. General theory of three-dimensional consolidation. J. Appl. Phys. 12, 155–164.
Biot, M.A., 1962. Mechanics of deformation and acoustic propagation in porous media. J. Appl. Phys. 33, 1482–1498.
Byrne, H., Chaplain, M.A., 1996. Modelling the role of cell-cell adhesion in the growth and development of carcinomas. Math. Comput. Modell. 24, 1–17.
Cheng, A.H.D., 2016. Poroelasticity, vol. 27. Springer.
Cowin, S.C., Doty, S.B., 2007. Tissue Mechanics. Springer Science & Business Media.
Cryer, C., 1963. A comparison of the three-dimensional consolidation theories of Biot and Terzaghi. Quart. J. Mech. Appl. Math. 16, 401–412.
Documentation, A., 2006. Version 6.6, abaqus.
Duck, F.A., 2013. Physical Properties of Tissues: A Comprehensive Reference Book. Academic Press.
Ehlers, W., Markert, B., 2001. A linear viscoelastic biphasic model for soft tissues based on the theory of porous media. J. Biomech. Eng. 123, 418–424.
Eshelby, J.D., 1957. The determination of the elastic field of an ellipsoidal inclusion, and related problems. In: Proceedings of the Royal Society of London A: Mathematical, Physical and Engineering Sciences. The Royal Society, pp. 376–396.
Fung, Y.C., 1993. Mechanical properties and active remodeling of blood vessels. In: Biomechanics. Springer, pp. 321–391.
Fung, Y.c., 2013. Biomechanics: Mechanical Properties of Living Tissues. Springer Science & Business Media.
Gibson, R., Gobert, A., Schiffman, R., 1989. On Cryer's problem with large displacements. Int. J. Num. Anal. Methods Geomech. 13, 251–262.
Islam, M.T., Chaudhry, A., Tang, S., Tasciotti, E., Righetti, R., 2018a. A new method for estimating the effective poisson's ratio in ultrasound poroelastography. IEEE Trans. Med. Imag. 37, 1178–1191.
Islam, M.T., Chaudhry, A., Unnikrishnan, G., Reddy, J., Righetti, R., 2018b. An analytical model of tumors with higher permeability than surrounding tissues for ultrasound elastography imaging. J. Eng. Sci. Med. Diagn. Therapy 1. 031006031006.
Islam, M.T., Chaudhry, A., Unnikrishnan, G., Reddy, J., Righetti, R., 2018c. An analytical poroelastic model for ultrasound elastography imaging of tumors. Phys. Med. Biol. 63, 025031.
Islam, M.T., Reddy, J., Righetti, R., 2018d. An analytical poroelastic model of a non-homogeneous medium under creep compression for ultrasound poroelastography applications – Part I. J. Biomech. Eng. (in press)
Islam, M.T., Reddy, J., Righetti, R., 2018e. An analytical poroelastic model of a non-homogeneous medium under creep compression for ultrasound poroelastography applications – Part II. J. Biomech. Eng. (in press)
Islam, M.T., Reddy, J., Righetti, R., 2018f. A model-based approach to investigate the effect of elevated interstitial fluid pressure on strain elastography. Phys. Med. Biol. 63, 215011.

Islam, M.T., Tang, S., Liverani, C., Tasciotti, E., Righetti, R., 2018g. Non-invasive imaging of the young's modulus and poisson's ratio of cancer tumor in vivo. arXiv preprint arXiv:1809.02929.
Jain, R.K., 1998. Delivery of molecular and cellular medicine to solid tumors. J. Controlled Release 53, 49–67.
Jain, R.K., Martin, J.D., Stylianopoulos, T., 2014. The role of mechanical forces in tumor growth and therapy. Ann. Rev. Biomed. Eng. 16, 321.
Jain, R.K., Tong, R.T., Munn, L.L., 2007. Effect of vascular normalization by antiangiogenic therapy on interstitial hypertension, peritumor edema, and lymphatic metastasis: insights from a mathematical model. Cancer Res. 67, 2729–2735.
Jones, A., Byrne, H., Gibson, J., Dold, J., 2000. A mathematical model of the stress induced during avascular tumour growth. J. Math. Biol. 40, 473–499.
Konofagou, E.E., Harrigan, T.P., Ophir, J., Krouskop, T.A., 2001. Poroelastography: imaging the poroelastic properties of tissues. Ultras. Med. Biol. 27, 1387–1397.
Kremheller, J., Vuong, A.T., Yoshihara, L., Wall, W.A., Schrefler, B.A., 2018. A monolithic multiphase porous medium framework for (a-)vascular tumor growth. Comput. Methods Appl. Mech. Eng.
Kyriacou, S.K., Davatzikos, C., Zinreich, S.J., Bryan, R.N., 1999. Nonlinear elastic registration of brain images with tumor pathology using a biomechanical model [MRI]. IEEE Trans. Med. Imag. 18, 580–592.
Lakes, R.S., 1998. Viscoelastic Solids, vol. 9. CRC Press.
Leiderman, R., Barbone, P.E., Oberai, A.A., Bamber, J.C., 2006. Coupling between elastic strain and interstitial fluid flow: ramifications for poroelastic imaging. Phys. Med. Biol. 51, 6291.
Mason, D., Solomon, A., Nicolaysen, L., 1991. Evolution of stress and strain during the consolidation of a fluid-saturated porous elastic sphere. J. Appl. Phys. 70, 4724–4740.
Mow, V., Bachrach, N., Setton, L., Guilak, F., 1994. Stress, strain, pressure and flow fields in articular cartilage and chondrocytes. In: Cell Mechanics and Cellular Engineering. Springer, pp. 345–379.
Mow, V.C., Kuei, S., Lai, W.M., Armstrong, C.G., 1980. Biphasic creep and stress relaxation of articular cartilage in compression: theory and experiments. J. Biomech. Eng. 102, 73–84.
Mow, V.C., Lai, W.M., 1980. Recent developments in synovial joint biomechanics. Siam Rev. 22, 275–317.
Mow, V.C., Ratcliffe, A., Woo, S.L., 2012. Biomechanics of Diarthrodial Joints, vol. 1. Springer Science & Business Media.
Mpekris, F., Baish, J.W., Stylianopoulos, T., Jain, R.K., 2017. Role of vascular normalization in benefit from metronomic chemotherapy. Proc. National Acad. Sci. 114, 1994–1999.
Nair, S.P., Yang, X., Krouskop, T.A., Righetti, R., 2011. Performance analysis of a new real-time elastographic time constant estimator. IEEE Trans. Med. Imag. 30, 497–511.
Netti, P.A., Baxter, L.T., Boucher, Y., Skalak, R., Jain, R.K., 1995. Time-dependent behavior of interstitial fluid pressure in solid tumors: implications for drug delivery. Cancer Res. 55, 5451–5458.
Netti, P.A., Baxter, L.T., Boucher, Y., Skalak, R., Jain, R.K., 1997. Macro-and microscopic fluid transport in living tissues: Application to solid tumors. AIChE J. 43, 818–834.
Netti, P.A., Berk, D.A., Swartz, M.A., Grodzinsky, A.J., Jain, R.K., 2000. Role of extracellular matrix assembly in interstitial transport in solid tumors. Cancer Res. 60, 2497–2503.
Ophir, J., Alam, S., Garra, B., Kallel, F., Konofagou, E., Krouskop, T., Varghese, T., 1999. Elastography: ultrasonic estimation and imaging of the elastic properties of tissues. Proc. Inst. Mech. Eng., Part H: J. Eng. Med. 213, 203–233.
Pflaster, D., Yuan, Y., Krag, I., 1996. A poroelastic finite element formulation including transport and swelling in soft tissue structures. J. Biomech. Eng. 118, 1.
Rice, J., Rudnicki, J., Simons, D.A., 1978. Deformation of spherical cavities and inclusions in fluid-infiltrated elastic materials. Int. J. Solids Struct. 14, 289–303.
Righetti, R., Garra, B.S., Mobbs, L.M., Kraemer-Chant, C.M., Ophir, J., Krouskop, T.A., 2007. The feasibility of using poroelastographic techniques for distinguishing between normal and lymphedematous tissues in vivo. Phys. Med. Biol. 52, 6525.
Righetti, R., Ophir, J., Srinivasan, S., Krouskop, T.A., 2004. The feasibility of using elastography for imaging the poisson's ratio in porous media. Ultras. Med. Biol. 30, 215–228.
Rzymski, P., Opala, T., 2011. Elastography as a new diagnostic tool to detect breast cancer–evaluation of research and clinical applications. Prz. Menopauzalny 5, 357–362.
Rzymski, P., Skórzewska, A., Opala, T., 2010. Changes in ultrasound shear wave elastography properties of normal breast during menstrual cycle. Clin. Exp. Obstet. Gynecol. 38, 137–142.
Sarntinoranont, M., Rooney, F., Ferrari, M., 2003. Interstitial stress and fluid pressure within a growing tumor. Ann. Biomed. Eng. 31, 327–335.
Sciumè, G., Santagiuliana, R., Ferrari, M., Decuzzi, P., Schrefler, B., 2014. A tumor growth model with deformable ECM. Phys. Biol. 11, 065004.
Sinkus, R., Tanter, M., Xydeas, T., Catheline, S., Bercoff, J., Fink, M., 2005. Viscoelastic shear properties of in vivo breast lesions measured by mr elastography. Magn. Reson. Imag. 23, 159–165.
Song, Y., Hu, H., Rudnicki, J.W., 2016a. Shear properties of heterogeneous fluid-filled porous media with spherical inclusions. Int. J. Solids Struct. 83, 154–168.
Song, Y., Hu, H., Rudnicki, J.W., Duan, Y., 2016b. Dynamic transverse shear modulus for a heterogeneous fluid-filled porous solid containing cylindrical inclusions. Geophys. J. Int. 206, 1677–1694.
Stapleton, S., Milosevic, M., Allen, C., Zheng, J., Dunne, M., Yeung, I., Jaffray, D.A., 2013. A mathematical model of the enhanced permeability and retention effect for liposome transport in solid tumors. PloS One 8, e81157.
Stylianopoulos, T., Martin, J.D., Snuderl, M., Mpekris, F., Jain, S.R., Jain, R.K., 2013. Coevolution of solid stress and interstitial fluid pressure in tumors during progression: implications for vascular collapse. Cancer Res. 73, 3833–3841.
Suh, J.K., DiSilvestro, M., 1999. Biphasic poroviscoelastic behavior of hydrated biological soft tissue. J. Appl. Mech. 66, 528–535.
Swabb, E.A., Wei, J., Gullino, P.M., 1974. Diffusion and convection in normal and neoplastic tissues. Cancer Res. 34, 2814–2822.
Swartz, M.A., Fleury, M.E., 2007. Interstitial flow and its effects in soft tissues. Annu. Rev. Biomed. Eng. 9, 229–256.
Swartz, M.A., Kaipainen, A., Netti, P.A., Brekken, C., Boucher, Y., Grodzinsky, A.J., Jain, R.K., 1999. Mechanics of interstitial-lymphatic fluid transport: theoretical foundation and experimental validation. J. Biomech. 32, 1297–1307.
Verruijt, A., 2013. Theory and Problems of Poroelasticity. Delft University of Technology.
Zhi, H., Ou, B., Luo, B.M., Feng, X., Wen, Y.L., Yang, H.Y., 2007. Comparison of ultrasound elastography, mammography, and sonography in the diagnosis of solid breast lesions. J. Ultras. Med. 26, 807–815.
Zhou, J., Smiatek, J., Asmolov, E.S., Vinogradova, O.I., Schmid, F., 2015. Application of tunable-slip boundary conditions in particle-based simulations. High Performance Computing in Science and Engineering, vol. 14. Springer, pp. 19–30.